

**Full Paper**

**Control of Pore Structure in Polymeric Monoliths Prepared from Colloidal Dispersions<sup>a</sup>**

Alberto Cingolani, Danilo Cuccato, Giuseppe Storti and Massimo Morbidelli\*

---

A. Cingolani, Prof. G. Storti, Prof. M. Morbidelli.

Institute for Chemical and Bioengineering, Department of Chemistry and Applied Bioscience  
ETH Zurich, Vladimir-Prelog-Weg 1-5/10, 8093 Zürich, Switzerland

E-mail: [massimo.morbidelli@chem.ethz.ch](mailto:massimo.morbidelli@chem.ethz.ch)

Dr. D. Cuccato

Imperial College London, South Kensington Campus, London, SW7 2AZ, United Kingdom

---

Reliable control of pore size distribution in porous materials is a key feature for addressing specific applications. The Reactive Gelation process represents a robust and efficient method to obtain mechanically stable monoliths with tunable pore size distribution. Primary polymer nanoparticles are destabilized and aggregated in a controlled way, forming a percolating gel. Afterwards, this structure is hardened by a post-polymerization, carried out through heating. Different parameters play a major role in determining the final morphology of the monolith. In this work, we investigate the effect of primary particle architecture (i.e. core-to-shell ratio) and initial solid content of the latex, using two different sizes of nanoparticles. Actually, the first parameter affects the pores in the small range (0.01-1  $\mu\text{m}$ ) whereas the latter those in the larger one (1 to several  $\mu\text{m}$ ), independently of the primary particle size. As a result, monoliths with very well defined pore size distributions are obtained.

---

<sup>a</sup> **Supporting Information** is available online from the Wiley Online Library or from the author.

## 1. Introduction

Porous polymers find important applications in various areas, ranging from biotechnology<sup>[1]</sup>, to energy storage<sup>[2]</sup>, catalysis<sup>[3]</sup> and adsorption separations<sup>[4]</sup>. In the latter case, porous particles<sup>[5]</sup> as well as monoliths<sup>[6,7]</sup> are used as major stationary phases in liquid chromatography. Such a variety of applications depends primarily on the very peculiar features of these materials, especially in terms of porous structures, since monodispersed<sup>[8]</sup> as well as hierarchical<sup>[9]</sup> arrangements of micro-, meso- and macro-pores can be obtained. Different strategies are available for the preparation of these materials<sup>[10]</sup>. The most common one implies the usage of a porogen for the formation of porous particles<sup>[10-12]</sup>. In addition, block-copolymer self-assembly<sup>[13]</sup> and post modification of resins, carried out generally via pyrolysis<sup>[14]</sup> or solvent exposure<sup>[15]</sup>, are also used. In all of these methods, many different, interlinked parameters affect the final product properties and the resulting structure, making often difficult the design and control of the process<sup>[10]</sup>.

As an alternative to the previously mentioned approaches, colloidal gelation<sup>[16,17]</sup> represents an original procedure to synthesize porous structures. Taking advantages of the fractal geometry of the micro-clusters<sup>[18]</sup> formed during the particle aggregation, eventually leading to a percolating network<sup>[19]</sup>, different porous frameworks can be obtained. These can be stabilized in structures exhibiting strong mechanical properties through the Reactive Gelation process<sup>[20]</sup>. This method comprises different subsequent steps: starting from a dispersion of polymer nanoparticles in water (the so-called latex), additional monomer and oil-soluble initiator are added in order to swell the particles. After aggregation, occurring because of suitable latex destabilization, the added monomer is further polymerized in order to form strong inter-particle bonds by means of connecting polymer chains, thus providing mechanical resistance to the previously achieved percolating structure. Using this technique, many different materials for liquid chromatography application, both in form of monoliths<sup>[21,22]</sup> as well as particles<sup>[23-25]</sup>

have been produced. The major advantage of this method resides in the possibility to tune and precisely control the size, composition, morphology, surface characteristics and functionalities of the primary particles which are prepared through the well-established emulsion polymerization<sup>[26]</sup>. Moreover, the aggregation process as well can be controlled playing with the latex properties (i.e., volume fraction or charge properties of the particle surface) and aggregation kinetics (i.e., electrolyte addition)<sup>[19]</sup>. All the aforementioned parameters concur to define the morphology of the final gel, resulting in a variety of final structures<sup>[18]</sup>. Upon post-polymerization, the final gel acquires remarkable mechanical properties and is then able to withstand solvent evaporation from the pores during ambient drying.

In this work we show quantitatively how to carefully control the porous structure in monolithic foams by properly acting on specific latex properties, namely particle architecture (core and shell composition and thickness), average particle size, and solid content of the latex. This way, the pore size distribution and morphology in polymer monoliths can be tuned across multiple length scale. This control directly reflects into the functional properties of the monoliths themselves in dependence of their final application. For example, in chromatography large pores make the mass transport dominated by convection, allowing high performance at very high flow rates<sup>7</sup>. Moreover, careful control of the individual pore sizes is desirable for size exclusion operations. On the other hand, in thermal insulation, smaller pores are required because they reduce the conductivity of the final material when compared to the mean-free-path of the contained molecules<sup>[27]</sup>.

## **2. Experimental Section**

### **2.1 Materials**

The following chemicals have been employed without further treatments: styrene (STY, 10-15 ppm 4-tert-butylcatechol as stabilizer, purity 99%) from ABCR-Chemicals (D-76187

Karlsruhe); divinylbenzene (DVB, technical grade, > 80%) and sodium dodecyl sulfate (SDS, purity  $\geq$  99%) from Sigma Aldrich; potassium peroxydisulfate (KPS) from Merck Millipore, 2,2'-azobis(2-methylpropionitrile) (AIBN, purity 98%) from Fluka Analytical; sodium chloride (for analysis, ACS, ISO, Reag. Ph Eur) from Emsure. Ultra-pure grade water was prepared by Millipore Synergy.

## **2.2 Reactive Gelation**

The procedure used to synthesize the porous monoliths is based on the following steps: initially, a polymer latex (colloidal dispersion of polymer particles in water) was synthesized via emulsion polymerization and subsequently monomer and oil-soluble initiator were added. Afterwards, the swollen nanoparticles were destabilized and aggregated in a controlled way via salt addition. Once the gel was formed, it was left overnight at 50°C inside an oven to complete the added monomer consumption by free radical polymerization. Finally, the monoliths were fully dried, enabling their complete morphological characterization. All of the aforementioned steps are described in details in the following.

### **2.2.1 Emulsion polymerization**

A semi-batch emulsion polymerization protocol was followed for the production of all the latexes. This procedure was divided into two subsequent steps, corresponding to the synthesis first of the core and then of the shell of the polymer particles. In particular, in the first phase a highly crosslinked (20%) seed of nanoparticles was produced and in the second one, a softer, less crosslinked (1%) shell was grown. Starting from a mixture (Initial Charge, IC) of water and surfactant (SDS) into a glass reactor, a solution (Initiator Shot 1, IS1) of water and initiator (KPS) was injected, once the temperature reached the set-point of 70°C. Afterwards, an emulsion of styrene, DVB, water, and surfactant (Charged Feed 1, CF1) was fed over the reaction time using an HPLC pump. Moreover, a solution of water and KPS (Initiator Feed, IF) was continuously fed as well, as the total reaction time is longer than the half-life time of the initiator at the reaction temperature. The reacting mixture was constantly monitored and

specifically conversion checked to ensure that the system is kept in starved condition. The previously synthesized latex acts as a seed for the growth of a soft shell around the hard core particles. A new monomer solution (Charged Feed 2, CF2), this time composed only of styrene and DVB, was then fed to the system in a continuous way (i.e., without lag time or stopping the previous reaction of core synthesis), in order to achieve a radially homogeneous shell growth. The previous initiator feed was disconnected, while a shot of water and KPS was added to the reaction to keep it proceeding (Initiator Shot 2, IS2). Also during this stage, the reacting mixture was constantly monitored in terms of conversion to ensure starved condition. After the new monomer addition was complete, the synthesis was stopped once full conversion and the desired particle size, determined as z-average value from dynamic light scattering measurements, were obtained. Further details and references on the synthesis of each latex are reported in the Supporting Information (SI).

### 2.2.2 Latex Swelling

The latex was diluted with deionized water to the desired dry solid content, measured through thermogravimetric analysis in a HG53 Halogen Moisture Analyzer from Mettler-Toledo. Afterwards, an additional amount of a mixture of divinylbenzene and AIBN (5 %wt with respect to the monomer) was added. Considering the much larger amount of cross-linker in the core than in the shell, it is reasonable to assume that this additional monomer swelled only the outer layer of the particles. This additional mixture amount was about 20 %wt with respect to the dry solid content of the particle shell. The solution was left under agitation at 200 rpm overnight to ensure equilibrium swelling.

### 2.2.3 Latex Gelation

The swollen latexes were aggregated by mixing with an equivalent volume of a salt solution within 4 ml vials. Typical gelation time is about 20 minutes. The vials were carefully closed before post-polymerization. The specific recipes of each produced monolith are reported in SI.

### 2.2.4 Gel Post-Polymerization and Drying

The formed gels inside the closed vials (**Figure S1** of Supplementary Information) were put into an oven at 50° C for at least 12 hours. After the reaction, they were still wet and quite fragile (the material cannot be easily handled – moved or touched – without damaging it). They were then transferred into a container with excess of water and left there (2-3 days) to remove residual non-aggregated particles and salt from the gel. Finally, the monoliths were dried in air, while their weight loss was checked daily to verify that full drying was achieved (the process takes ca. 3-5 days).

### 2.3 Monolith Characterization

The pore size distributions of the dry monoliths have been measured by mercury intrusion porosimetry (Hg Intrusion) using the instruments Pascal 140 and Pascal 440 from Thermo Scientific. Further investigation of the monolith structure and surface were performed by scanning electron microscopy (SEM) using a Gemini 1530 FEG from Zeiss with field emission gun operated at 5 kV. Surface area measurements were performed via nitrogen adsorption (BET theory) using TriStar 3000 from Micromeritics. Finally, the total porosity was estimated by measuring the skeletal density of the sample and comparing it with the one of the fully non-porous materials. In particular, each dry sample was weighted first, then put into a container filled with isopropyl alcohol and left for 24 hours to achieve complete penetration of the solvent into the pores. Each sample impregnated by the alcohol (IPA-wet foam) was weighted again to evaluate the mass of alcohol intruded into the pores. The total porosity of each samples ( $\varepsilon$ ) was then evaluated as follows:

$$\varepsilon = \frac{(m_{wet} - m_{dry}) / \rho_{IPA}}{\frac{m_{wet} - m_{dry}}{\rho_{IPA}} + \frac{m_{dry}}{\rho_{PS}}} \quad (1)$$

where  $\rho_{PS}$  and  $\rho_{IPA}$  are the densities of polystyrene and IPA, respectively, while  $m_{wet}$  and  $m_{dry}$  are the masses of IPA-wet and dry samples, respectively ( $\rho_{PS} / \rho_{IPA} = 1.325$ ). Fifteen different measurements have been repeated for each monolith and average values with standard deviation

have been computed. The obtained results have been compared with those obtained through Hg intrusion in order to cross-check the results.

### **3. Result and Discussion**

#### **3.1 The Reactive Gelation Process**

During the first step of the process the particles are destabilized by electrolyte addition in the stagnant dispersion and aggregation proceeds until the resulting fractal clusters occupy all of the available space and their movement is hindered (arrest time). At this point they start interconnecting with each other, forming a percolating structure. The whole process is controlled by the electrolyte concentration in solution, leading to different aggregation regimes, namely DLCA (diffusion limited cluster aggregation) and RLCA (reaction limited cluster aggregation)<sup>[19]</sup>. Considering the swelling of the outer layer of the particles, which reduces considerably the glass transition temperature ( $T_g$ ) of the polymer<sup>[28]</sup>, it is reasonable to assume that they partly interpenetrate depending upon the shell thickness<sup>[29]</sup>. Particles with small core-to-particle ratio will interpenetrate more than those with larger ratios if the characteristic time of the gelation process is small enough compared to that of partial coalescence. Once the gel is heated up in the oven, the monomer in the outer layer of the particles starts polymerizing and, at the same time, particle rearrangement takes place, thus resulting in monolith shrinking. A second shrinking takes place during drying because of the evaporation of the capillary water<sup>[30]</sup>. Being the resulting porous framework affected by the combination of all the above processes, many parameters play a role in the process. In the following, the effects of particle core-shell morphology (architecture) and initial latex dry content are investigated.

#### **3.2 Effect of Particle Architecture**

To investigate the effect of particle architecture on the final pore structure of the monoliths, different latexes have been synthesized, as shown in **Table 1**. The ratio of the core to the particle

size,  $R_{CP}$ , and the actual size of the particles are changed. The dry content of the initial latex has been set equal to 8 %wt in all cases and all monoliths have been produced by mixing equivalent amounts of latex and salt solution, thus achieving RLCA conditions. Total porosity and surface area values of the obtained monoliths are summarized in **Table 2**.

### 3.2.1 Large Particles

Let us focus on the monoliths synthesized from the largest particles, i.e., M1, M2 and M3. As mentioned above, the monoliths are formed by salt addition, waiting until full percolation. All monoliths shrink during post-polymerization and larger shrinkage is found for structures formed from particles with smaller core-to-particle ratio. Remarkably, almost no shrinkage was observed for the case of the thinnest shell, sample M3. This means that the shell thickness, i.e., the amount of post-polymerized monomer, affects the rearrangement.

After the drying step, the final monoliths shown in **Figure 1** are obtained. This time, the trend is opposite to that observed for the previous process step: the monolith formed from particles with a small core-to-particle ratio (M1) retained its volume much better than M2, which instead shrank considerably. Moreover, the monolith M3 was not mechanically stable and broke into fragments while drying. It is worth repeating that each gel was formed mixing the latex with an equal volume of salt solution at well-defined concentration (details in **Table S5** of SI): the collapse or major modification of the structure occurred afterwards, during the drying phase, where the shell thickness of the particle has much larger influence on the final structure than the gelation itself. Thicker shells allow in fact for deeper particle-particle interpenetration during aggregation thus providing better mechanical stability to the monolith, which therefore can better keep its structure during drying. On the other hand, thinner shells reduce the extent of interpenetration, thus leading to more fragile structures. Therefore, these gels need more rearrangement during drying to find a stable structure: this was the case of sample M2 while the interpenetration was not enough for sample M3 and the structure collapsed. These considerations are supported by the SEM pictures shown in **Figure 2** where the different extents

of interpenetration are clearly identified moving from the sample M1, in which the identity of the single primary particles is lost (Figure 2a), to M3, where the individual particles are still clearly recognizable (Figure 2c). The sample M2 (Figure 2b) lies clearly somewhere in between. The previous discussion directly reflects also into the possible final applications, as an intermediate processing of the monolith would anyhow be required before use. Indeed, actions like press-fitting into proper housing for chromatography<sup>22</sup> and general material handling in the form of huge thermal insulation panels, require suitable mechanical stability. The pore size distributions of monoliths M1 and M2 measured by Hg intrusion are shown in **Figure 3**. The difference between the two is evident: sample M1 exhibits bimodal pore size distribution, whereas M2 a quite broad monomodal one. Latex L1 enabled the preservation of large pores, with diameter up to 10 micrometers, while the smallest pore, those among individual nanoparticles, disappeared by coalescence. On the other hand, latex L2 did not allow large pores to remain in the final monolith, since they are most probably lost during drying and shrinking, while small pores are present even in the range of few nanometers. Note that the two materials are quite different in terms of total porosity, with monolith M1 exhibiting much larger pore volume (Table 2).

These results can be explained as follows: since both samples percolated occupying the same volume, with identical particle size and concentration, their initial gel structure (*i.e.*, right after stagnant gelation) is rather similar, with possible minor discrepancies due to the different shell thickness. The bimodal pore structure formed during gelation originates from two processes: the first one refers to the initial aggregation of the primary particles, leading to aggregation characterized by a well-defined fractal dimension (in the order of 1.9 – 2.2) which is responsible for the small inter-particles pores (0.01 to 1  $\mu\text{m}$ ), and the second one, which refers to the final cluster interpenetration and interconnection during the percolation phase, responsible for the large inter-clusters pores (1 to several  $\mu\text{m}$ ). The capability of the monolith to maintain this bimodal structure during post-polymerization and drying, mainly dependent on the primary

particle architecture, determines the final pore structure: smaller pores tend to disappear under the effect of partial coalescence, which is the case of sample M1, while less interpenetration makes the structure less stable, leading to a loss of large inter-cluster pores and preserving the inter-particle ones.

The measured values of specific surface area confirm the different interpenetration of the primary particles shown in the SEM pictures as well as the contribution of small pores ( $< 0.1 \mu\text{m}$ ) measured via Hg intrusion. As shown in Table 2, the lower the thickness of the shell, the larger is the value of the measured surface area.

### 3.2.2 Small Particles

In order to check whether the effect of the particle architecture is affected by the particle size, let us consider the monoliths produced from latexes with small particles, M4 and M5 in Table 2. Notably, the shrinkage is again determined by the ratio  $R_{CP}$ , which in turn controls the restructuring upon post-polymerization and drying (**Figure 4**). Samples made from particles with equal core-to-particle ratio shrank equivalently.

Also the pore size distribution is again determined by  $R_{CP}$  or shell thickness, as it appears from the curves referred to the samples produced with smaller particles and measured by Hg intrusion shown in **Figure 5**. Both the differential and cumulative pore size distributions are similar to those discussed for larger particles and the same conclusions can be drawn also for this case. In particular, a detailed comparison is shown in **Figure 6** in the cases of samples made from latexes with the same  $R_{CP} = 0.73$ . It is seen that smaller primary particles lead to smaller inter-particle pores, as indicated by the shift of the first peak in the pore size distribution from approximately 600 nm for particles with total size of 110 nm to about 150 nm for particles with total size of 56 nm. In both monoliths the largest pores (from 1  $\mu\text{m}$  to 10  $\mu\text{m}$ ) are preserved, even though the actual position of the peak corresponds to smaller pore size for smaller particles. This effect is mainly driven by the crowding of the particles more than by their size, since the identical dry content for the two starting latexes leads to different particle concentration in the final volume.

In the case of primary particles with  $R_{CP} = 0.82$ , the particle size effect becomes irrelevant, as shown in **Figure 7**. Indeed, only the largest pores are slightly affected by the previously mentioned particle crowding.

The data in Table 2 show that the reduction of total porosity upon shrinkage is observed also for smaller particles. Indeed, monoliths M4 and M5 exhibit a difference in porosity of 6.1% (Table 2), similarly to the case of large particles. Furthermore, the porosity values are also quite similar for particles with equivalent core-to-particle ratio (e.g. compare the values for samples M4 and M1). Not surprisingly, materials with similar pore size distribution, exhibit also similar total porosity values (cf. samples M2 and M5).

The values of specific surface area, shown in Table 2, reflect the different interpenetration of the primary particles already shown in the SEM pictures as well as the fraction of small pores, namely below 0.1  $\mu\text{m}$ , measured by intrusion techniques. In particular, the lower the thickness of the shell, the higher the value of the measured surface area, e.g. M4 presents a specific surface area smaller than M5. Not surprisingly, the value is larger for smaller particles.

### **3.3 Effect of initial dry content**

It was found that latexes composed of nanoparticles with smaller core-to-particle ratio ( $R_{CP} = 0.73$ ) can preserve the percolation structure obtained during the gelation process, independently of the initial nanoparticle size. This behavior has been observed also for different initial concentrations of primary particles still keeping the monolith volume equal to that of the same container. Therefore, the porosity of the final volume is strongly affected by the dry content of the initial latex. On the other hand, particles with  $R_{CP} = 0.82$  suffered major restructuring upon drying and the dry content effect might be less relevant. To study the impact of the solid content, different monoliths have been produced starting from latexes L1 and L2 at different dry contents as summarized in Table 3. Since the two sets of monoliths have been prepared from the same primary particles, the specific surface remains constant and BET measurements have not been run.

### 3.3.1 Core-to-particle ratio 0.73

Let us consider first the monoliths with larger shell thickness M6, M1, and M7 in **Table 3**. The pore size distributions of the different samples are shown in **Figure 8**. All of them look bimodal, with a first peak approximately at 0.6 - 0.8  $\mu\text{m}$  and a second one at much larger values of pore size, whose value is a function of the solid content i.e. 1.5  $\mu\text{m}$  for sample M6, 4  $\mu\text{m}$  for 1, and 9  $\mu\text{m}$  for M7. Remarkably, the area of the second peak increases with decreasing of the initial dry content of the latex. This behavior can be explained considering the mechanism of gel formation: at the beginning of the process, particle aggregation proceeds and fractal clusters are formed. Small pores are generated as interstitial spaces among the primary nanoparticles, that is the inter-particle pores corresponding to the left peaks in Figure 8. As seen above, those pores are affected by the interpenetration due to the shell softness and not by occupied volume within the container as well as by the dry content. Once the system is crowded, the clusters start interpenetrating each other and percolation occurs. This mechanism is responsible for the formation of larger pores, that is the inter-cluster pores, corresponding to the right peaks in Figure 8. At this stage, the initial dry content becomes the crucial factor: samples produced with smaller dry content, exhibited much larger inter-cluster pores and lower mechanical resistance. The corresponding overall porosity values are shown in Table 3. Reducing the dry content increases the porosity of the final dry monolith, especially when the shape is retained upon drying. While such increase is quite relevant when the solid content decreases from 12% to 8%, it is less relevant from 8% to 4%. This result is not surprising since there should exist anyhow a limit value of porosity for which the monolith can actually be produced. As a matter of fact, it is quite difficult to observe the gelation process with dry content lower than 4%.

### 3.3.2 Core-to-particle ratio 0.82

In this case (samples M8 and M2 in Table 3), the effective shrinkage was much more relevant than in the case of particles with thicker shell discussed above.

The pore size distributions of the different samples are shown in **Figure 9**. After shrinkage, the initial percolation structure is lost in both cases and only the smallest inter-particles pores are retained. This means that, independently on the initial dry content, a major rearrangement takes place in order to find an equilibrium during drying, which results in the loss of the largest pores. Therefore, the dry content has no effect on the morphology of the final monolith when particles with high enough core-to-particle ratio are used.

Looking at the total porosity values in Table 3, it appears that the overall porosity of the sample decreases by decreasing the solid content of the initial latex. The difference in porosity between the two monoliths, equal to 11.4 %, is quite similar to that of latexes with  $R_{CP} = 0.73$ , equal to 9.5%, thus confirming the important role played by the solid content on porosity independently of the particle architecture.

#### **4. Conclusion**

The preparation of different monoliths via reactive gelation of core-shell colloidal polymer particles has been investigated as a function of two major process parameters: the particle architecture, namely the soft shell thickness compared to the total particle size, and the initial solid content of the polymer latex.

A thick shell is crucial in determining the pore morphology of the final product. Monoliths characterized by bimodal pore size distribution and up to 10% larger porosity have been formed from particles with lower core-to-particle ratio (0.73), whereas monomodal pore size distribution and smaller porosity have been obtained at a higher core-to-particle ratio (0.82). Further increase in the core-to-particle ratio resulted in unstable structures due to very weak particle interconnections. In addition, increasing the shell thickness led to smaller surface areas, with a reduction of approximately 50% when passing from particles with  $R_{CP} = 0.82$  to 0.73. The effect of particle architecture on the pore size of the monoliths has been also investigated

using smaller particles (total particle size reduced by a factor of 2 while keeping constant the core-to-particle ratios), and the same conclusions were drawn. Therefore, we can conclude that particle architecture, namely core-to-particle ratio, affects the porous properties of the final monolith in a way which is rather independent on particle size.

About the solid content, provided that the right architecture is chosen, highly porous monoliths can be produced by properly decreasing the initial dry solid content.

The latex parameters investigated in this work (i.e. size, architecture, and solid content of the particles in the initial aqueous dispersion) represent a very valuable tool to control the process of monolith formation and its final porous structure. Consequently, reactive gelation appears as a very promising technique for the production of porous materials with specific pore size distribution and morphology, which may suit different kinds of applications.

## Supporting Information

Supporting Information is available from the Wiley Online Library or from the author.

Acknowledgments: The authors are thankful to Annette Röthlisberger and Michael Plötze for the help with the Mercury Intrusion measurements. Moreover, we thank Anna Beltzung and Antoine Klaue for the help with the BET measurements and the SEM pictures, respectively. Fruitful discussion with Dr. Hua Wu, Prof. Paolo Arosio and Prof. Marco Lattuada are also gratefully acknowledged.

Keywords: porous materials, porosity control, polymer, polymer nanoparticles

### References

- [1]. H.P. Hentze, M. Antonietti, *Rev. Mol. Biotechnol.* **2002**, *90*, 27–53.
- [2]. A. Magistris, E. Quartarone, P. Mustarelli, Y. Saito, H. Kataoka, *Solid State Ionics* **2002**, *152*, 347–354.
- [3]. P. Kaur, J. T. Hupp, S.T. Nguyen, *ACS Catal.* **2011**, *1*, 819–835.
- [4]. W. Lu, D. Yuan, D. Zhao, C. I. Schilling, O. Plietzsch, T. Muller, S. Bräse, J. Guenther, J. Blümel, R. Krishna, Z. Li, H. Zhou., *Chem. Mater.* **2010**, *22*, 5964–5972.
- [5]. M. T. Gokmen, F. E. Du Prez, *Prog. Polym. Sci.* **2012**, *37*, 365–405.
- [6]. I. Nischang, *J. Chromatogr. A* **2013**, *1287*, 39–58.
- [7]. G. Guiochon, *J. Chromatogr. A* **2007**, *1168*, 101–168.
- [8]. D. Maniglio, Y. Ding, L. Wang, C. Migliaresi, *Polymer.* **2011**, *52*, 22, 5102–5106.
- [9]. S. A. Saba, M. P. S. Mousavi, P. Bühlmann, M. A. Hillmyer, *J. Am. Chem. Soc.* **2015**, *137*, 28, 8896–8899.
- [10]. F. Svec, *J. Chromatogr. A*, **2010**, *1217*, 902–924.
- [11]. F. Maya, F. Svec, *Polym. (United Kingdom)* **2014**, *55*, 1, 340–346.

- [12]. F. Svec, J. M. Frechet, *J. Chem. Mater.* **1995**, 7, 6, 707–715.
- [13]. B. H. Jones, T. P. M. Lodge, *ACS Nano* **2011**, 5, 11, 8914–8927.
- [14]. S. Valkama, A. Nykänen, H. Kosonen, R. Ramani, F. Tuomisto, P. Engelhardt, G. Brinke, O. Ikkala, J. Ruokolainen, *Adv. Funct. Mater.* **2007**, 17, 2, 183–190.
- [15]. J. H. Chen, E. Ruckenstein, *J. Appl. Polym. Sci.* **1992**, 45, 3, 377–386.
- [16]. D. F. Schmidt, C. Du Fresne Von Hohenesche, A. Weiss, V. Schädler, *Chem. Mater.* **2008**, 20, 2851–2853.
- [17]. T. R. Cuadros, J. M. Aguilera, *Food Biophys.* **2015**, 10, 487–499.
- [18]. S. Lazzari, L. Nicoud, B. Jaquet, M. Lattuada, M. Morbidelli, *Adv. Colloid Interface Sci.* **2016**, 235, 1–13.
- [19]. H. Wu, M. Morbidelli, *Particuology* **2014**, 14, 1–11.
- [20]. N. Marti, F. Quattrini, A. Butté, M. Morbidelli, *Macromol. Mater. Eng.* **2005**, 290, 221–229.
- [21]. M. Bechtle, A. Butté, G. Storti, M. Morbidelli, *J. Chromatogr. A* **2010**, 1217, 4675–4681.
- [22]. B. Brand, M. Krättli, G. Storti, M. Morbidelli, *J. Sep. Sci.* **2011**, 34, 2159–2163.
- [23]. A. Lamprou, A., I. Köse, Z. Peña Aguirre, G. Storti, M. Morbidelli, M. Soos, *Langmuir* **2014**, 30, 46, 13970–13978.
- [24]. B. Coquebert De Neuville, A. Lamprou, M. Morbidelli, M. Soos, *J. Chromatogr. A* **2014**, 1374, 180–188.
- [25]. B. Brand, M. Morbidelli, M. Soos, *Langmuir* **2015**, 31, 46, 12727–12735.
- [26]. S. C. Thickett, R. G. Gilbert, *Polymer (Guildf)*. **2007**, 48, 6965–6991.
- [27]. L. W. Hrubesh, R. W. Pekala, *J. Mater. Res.* **1994**, 9, 731–738
- [28]. S. Chow, *Macromolecules* **1980**, 364, 12, 362–364.
- [29]. P. Arosio, D. Xie, H. Wu, L. Braun, M. Morbidelli, *Langmuir*, **2010** 26, 9, 6643–6649.
- [30]. D. M. Smith, P. J. Davis, *Charact. Porous Solids II* **1991**, 301–310.

*Figure 1.* Dried monoliths synthesized from different latexes



*Figure 2.* SEM pictures of the monoliths formed from samples M1 (a), M2 (b) and M3 (c)

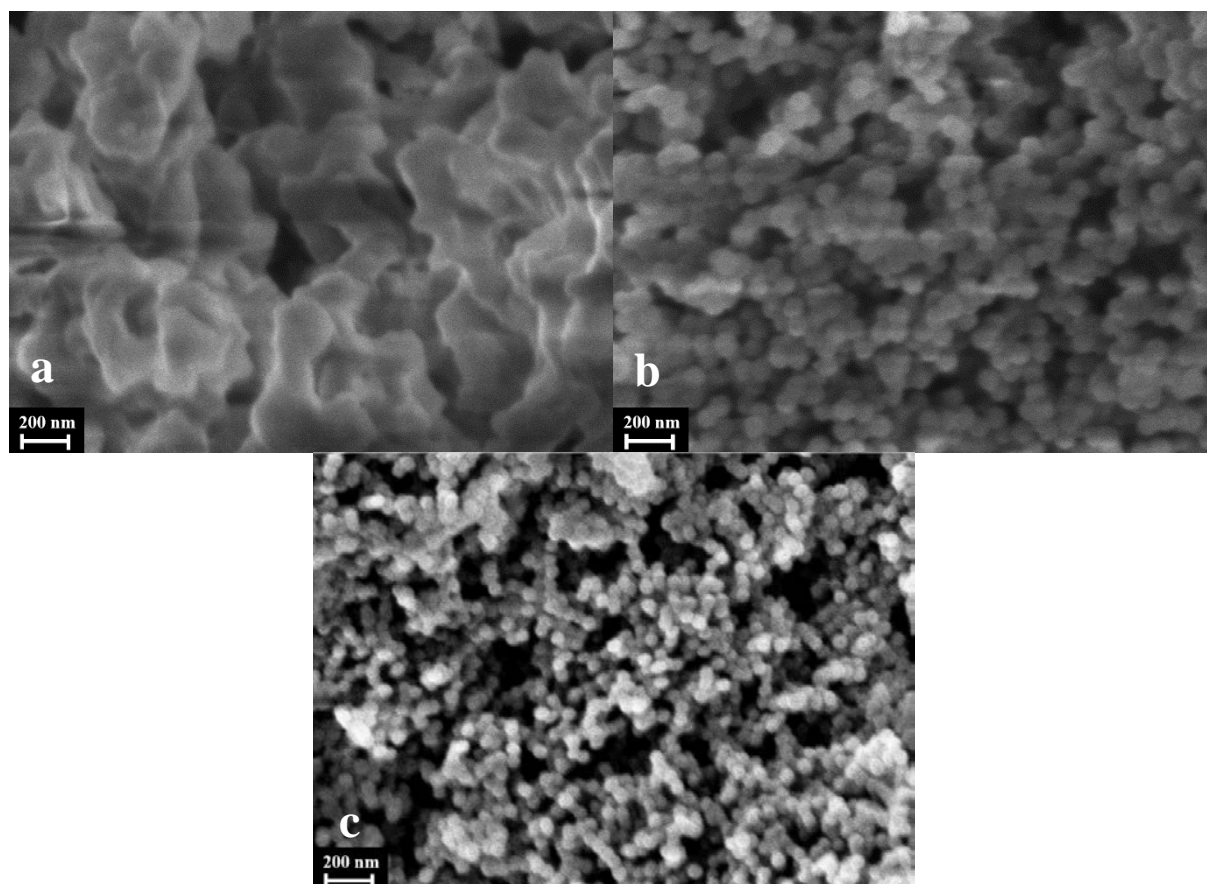
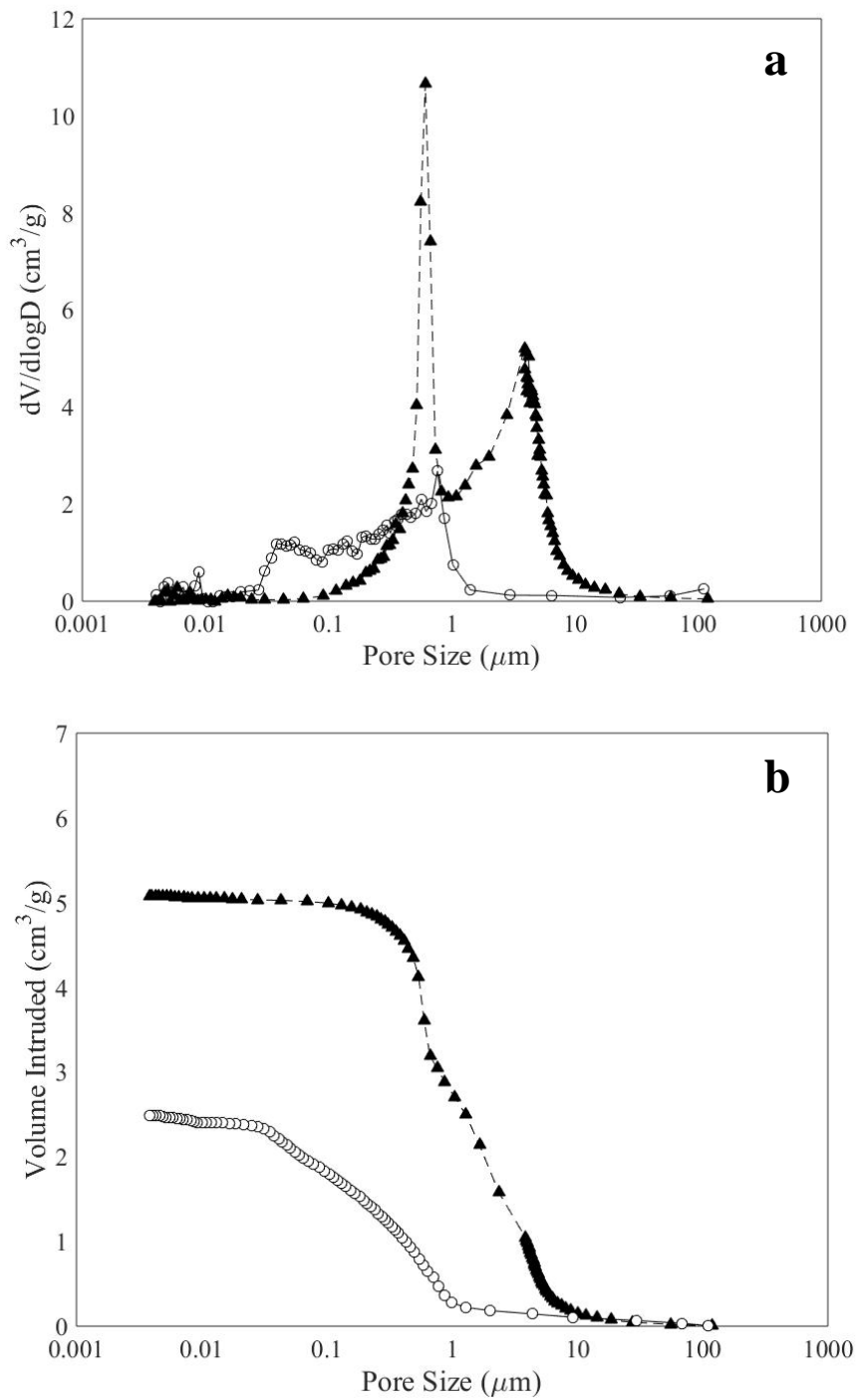


Figure 3. Differential (a) and cumulative (b) pore size distribution of the monoliths M1 (filled triangle) and M2 (empty circles)



*Figure 4.* Dried monoliths synthesized from different latexes presenting equivalent particle size (L5 and L4, L1 and L2) or equivalent particle architecture (L4 and L1, L5 and L2)

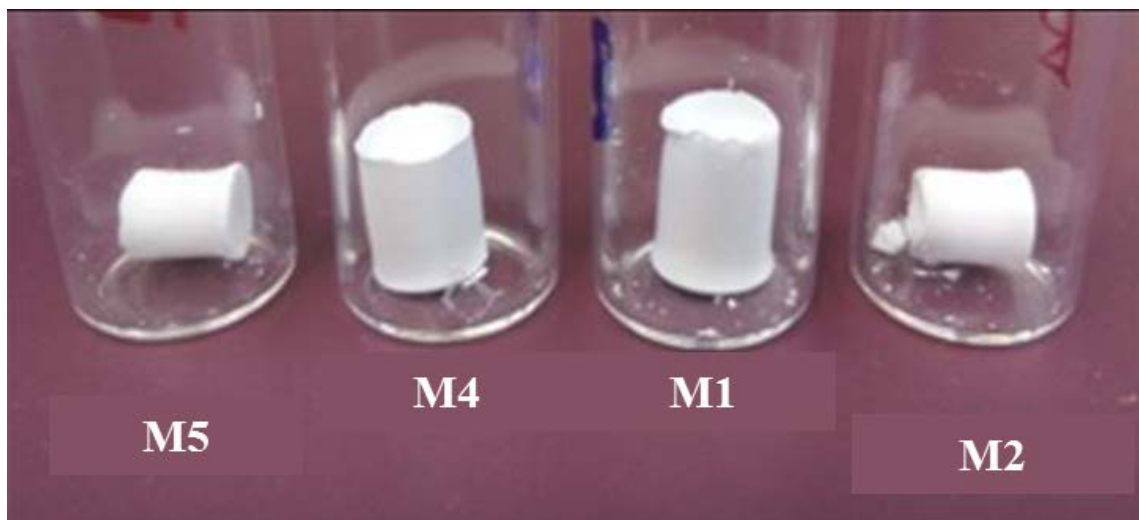


Figure 5. Differential (a) and cumulative (b) pore size distribution of the monoliths M4 (white triangle) and M5 (black circles)

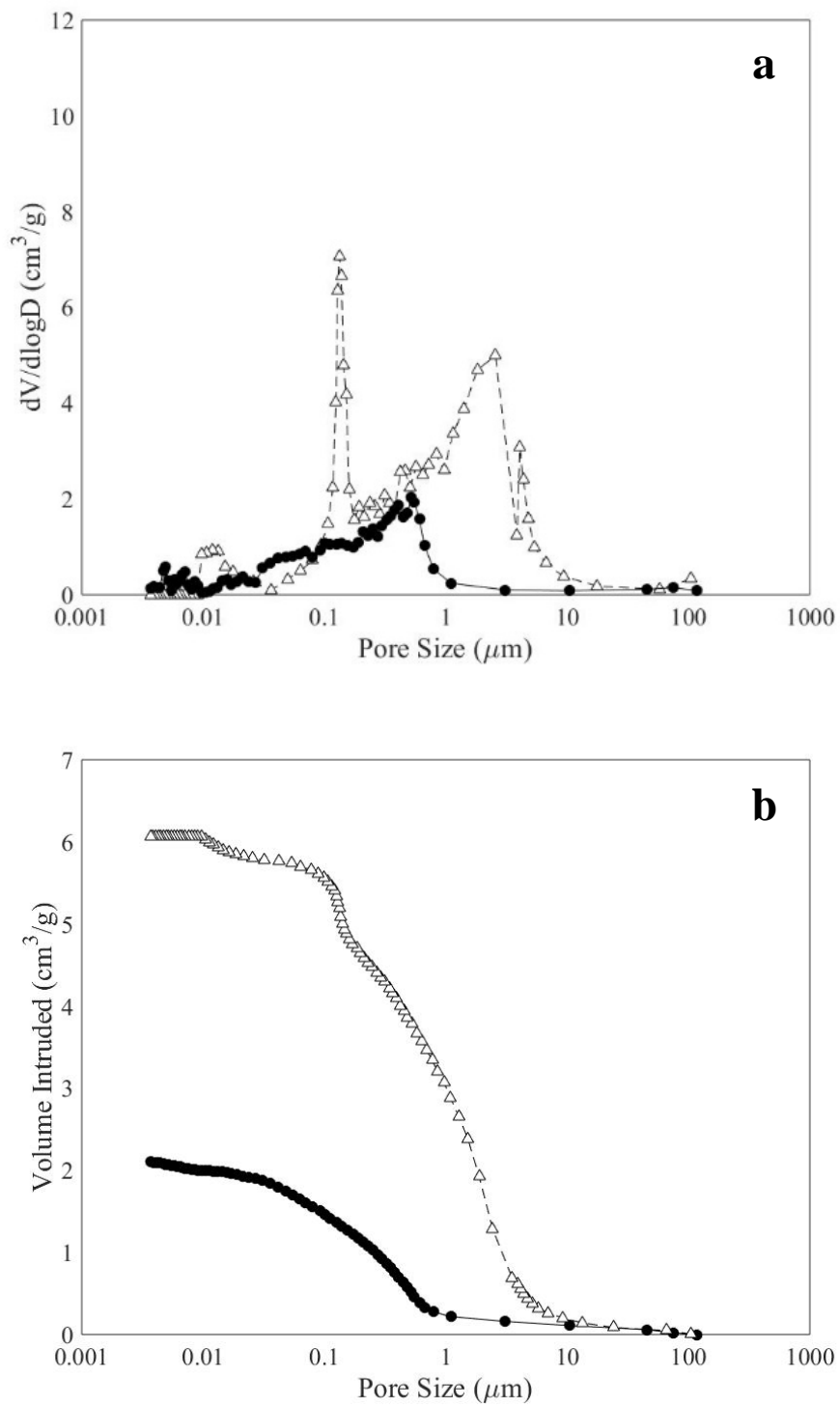


Figure 6. Differential (a) and cumulative (b) pore size distribution of the monoliths M4 (white triangle) and M1 (black triangle)

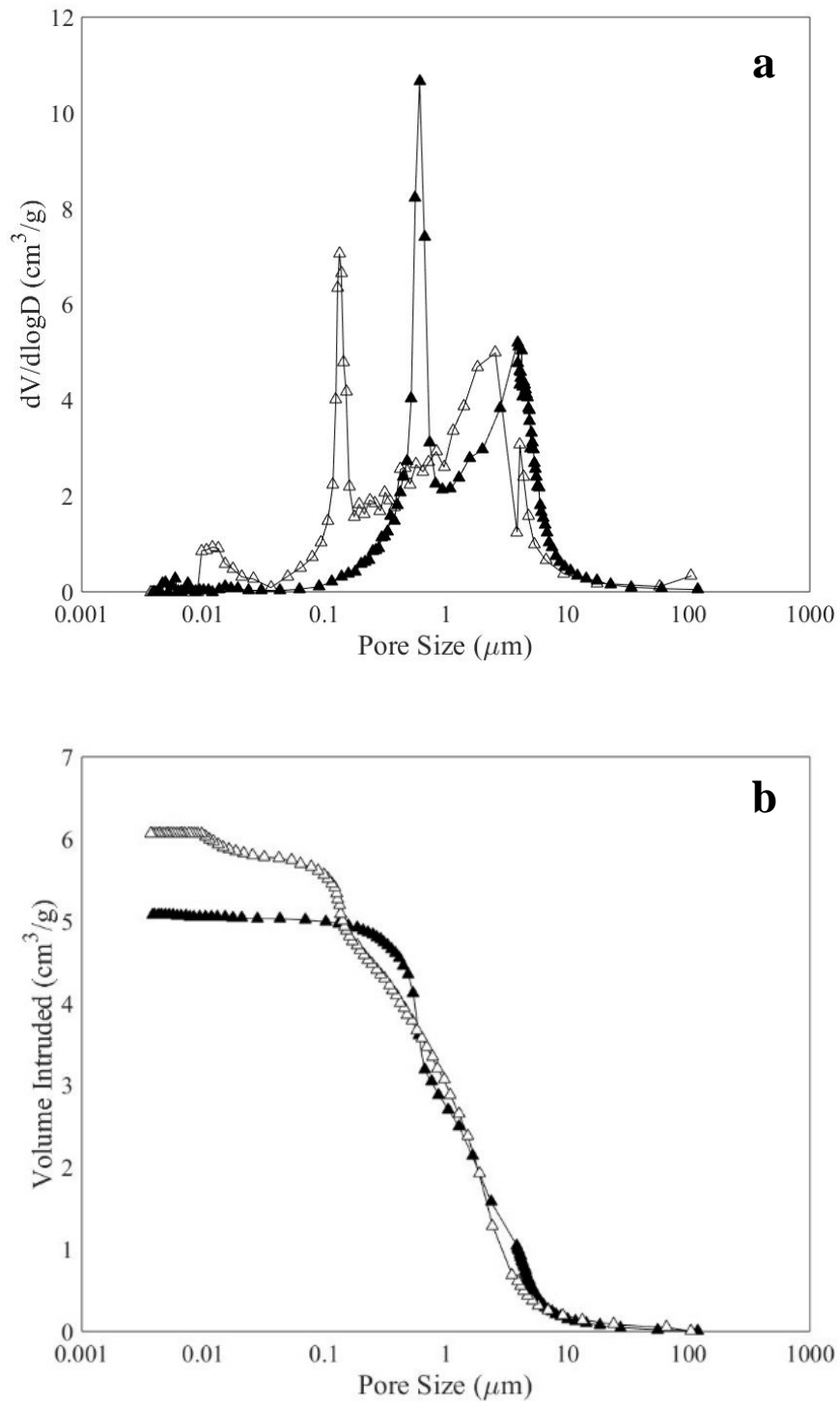


Figure 7. Differential (a) and cumulative (b) pore size distribution of the monoliths M5 (black circles) and M2 (white circles)

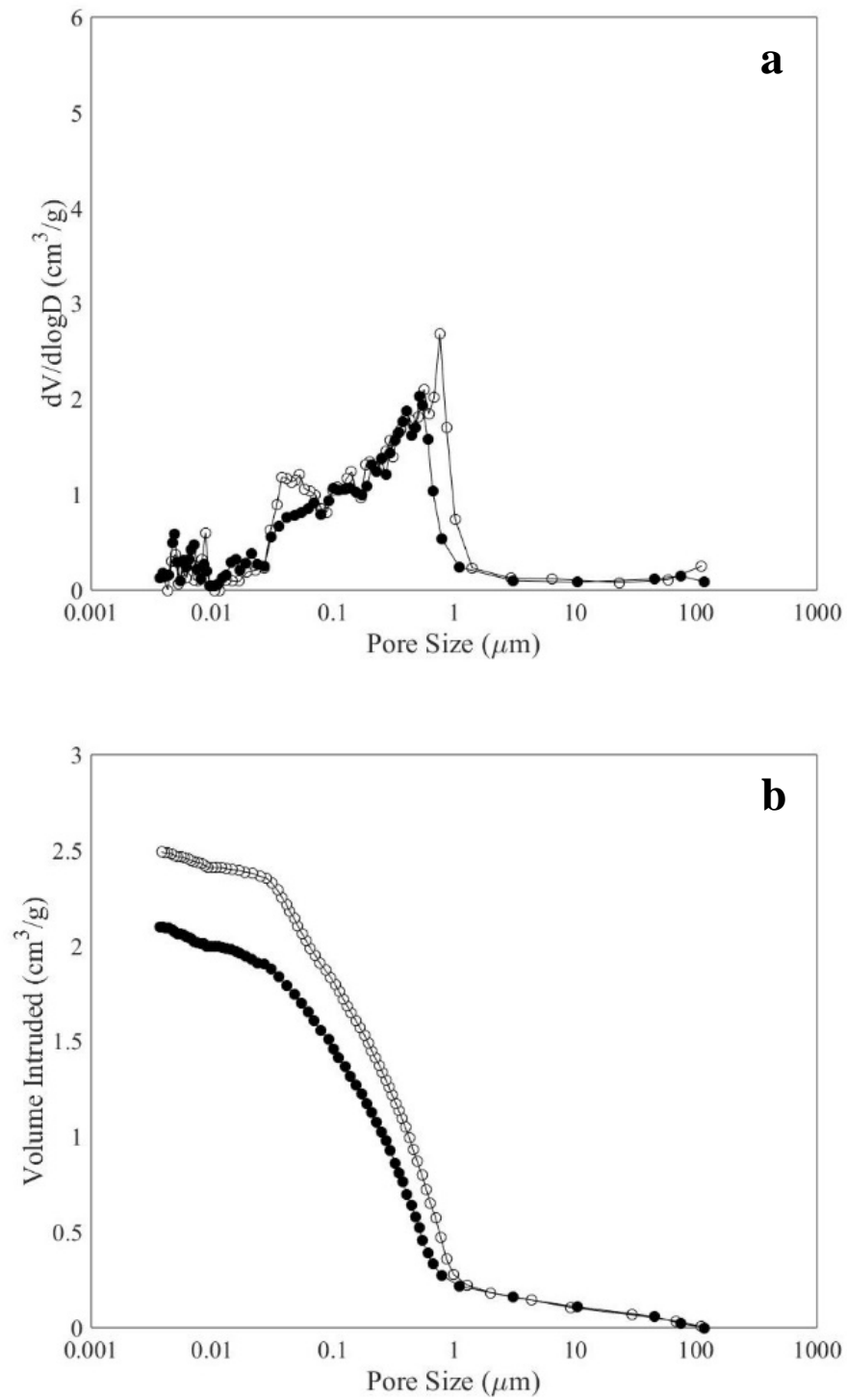


Figure 8. Differential (a) and cumulative (b) pore size distribution of the monoliths M6 (white circles), M1 (black triangles) and M7 (white squares).

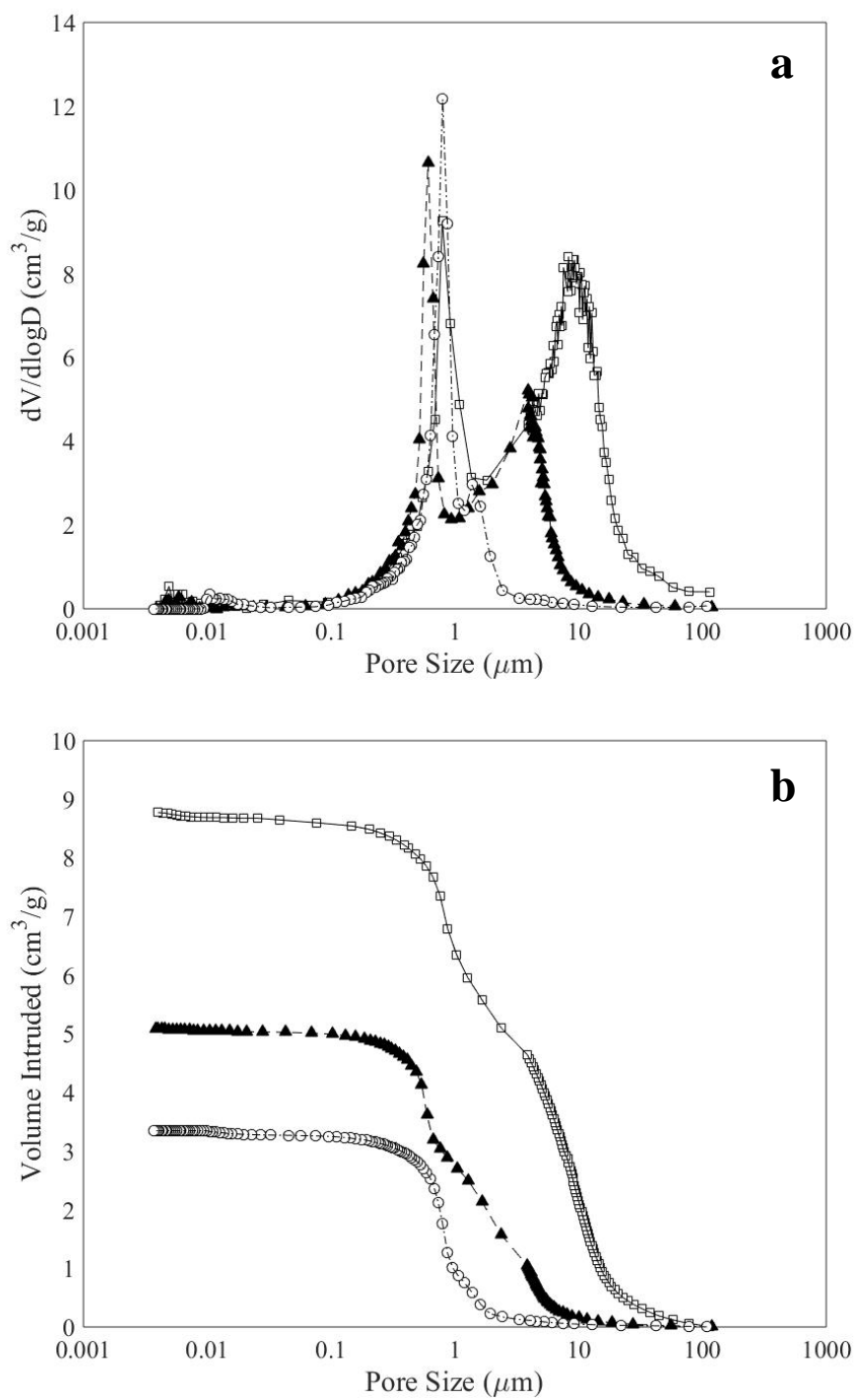


Figure 9. Differential (a) and cumulative (b) pore size distribution of the monoliths M8 (black squares) and M2 (white circles)

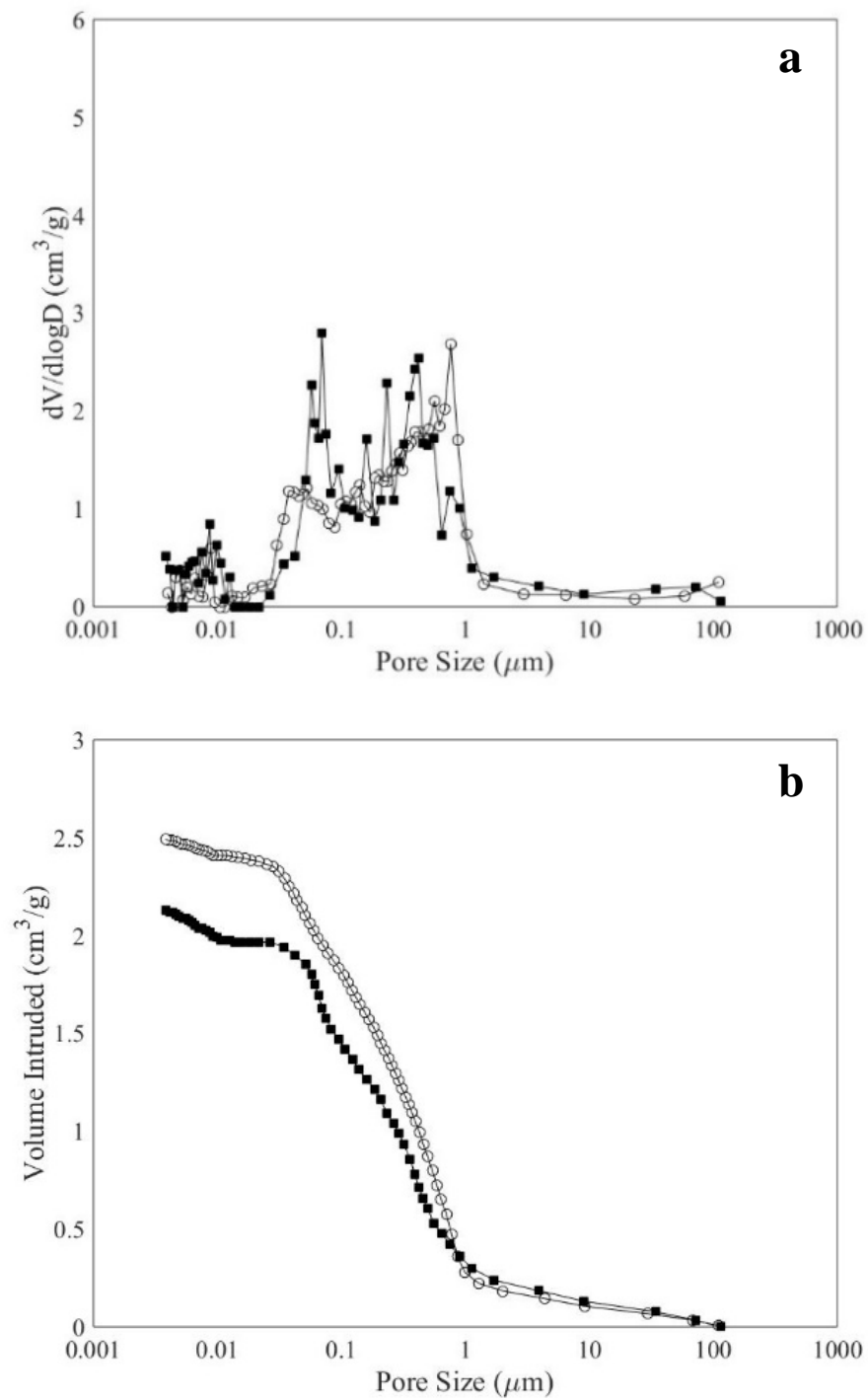


Table 1. Particle architecture of the different latexes

Latex	Core size [nm]	Particle size [nm]	$R_{CP}^b$
L1	80	110	0.73
L2	90	110	0.82
L3	100	110	0.91
L4	41	56	0.73
L5	40	49	0.82

Table 2. Total porosity and surface area of the produced monoliths

Sample	Total Porosity [%]	Surface Area [m <sup>2</sup> /g]
M1	86.6 ± 0.3%	17.37
M2	79.5 ± 2.6%	36.1
M3	-	58.69
M4	83.9 ± 0.3%	28.17
M5	77.8 ± 0.7%	58.76

Table 3. Characteristics of the monoliths produced at different dry contents

Sample	Latex	Initial dry content [w/w]	Porosity [%]
M6	L1	0.12	77.1 ± 1.0%
M1	L1	0.08	86.6 ± 0.3%
M7	L1	0.04	89.5 ± 0.4%
M8	L2	0.12	68.1 ± 0.1%
M2	L2	0.08	79.5 ± 2.6%

<sup>b</sup> Ratio of the core to the particle size